Effect of rare earth additions on the critical resolved shear stresses of magnesium alloys

V. Herrera-Solaz , P. Hidalgo-Manrique , M.T. Pérez-Prado , D. Letzig , J. Llorca , J. Segurado

ABSTRACT

An inverse optimization strategy based on crystal plasticity finite element simulations of polycrystals was used to obtain the critical resolved shear stresses of two Mg–1%Mn alloys containing neodymium from macroscopic experimental data. It was found that, with respect to pure Mg, the presence of Nd increases the $CRSS_{basal}$, $CRSS_{twinning}$, and the $CRSS_{basal}/CRSS_{twinning}$ ratio and decreases the $CRSS_{non\text{-}basal}/CRSS_{twinning}$ ratio. Additions of neodymium as high as 1 wt% result in similar CRSSs values for all deformation modes and, thus, in an isotropic yielding behavior.

Magnesium (Mg) alloys deform by crystallographic slip along certain directions on basal, prismatic and pyramidal planes and by mechanical twinning [1]. The ease of activation of each deformation mechanism is related to the corresponding critical resolved shear stress (CRSS). It is generally accepted that $CRSS_{basal} < CRSS_{twinning} < CRSS_{prismatic} < CRSS_{pyramidal}$ at low temperatures [2]. Moreover, the relative activity of each deformation mechanism is highly dependent on texture due to the small number of independent slip systems [3]. This anisotropy is further accentuated by the polar nature of twinning [4] which, for a given texture, may lead to different activities of the available deformation systems in tension and compression, giving rise to a yield asymmetry [5]. Wrought Mg alloys exhibit a particularly pronounced yield stress anisotropy and asymmetry at room temperature (RT) due to their sharp crystallographic textures [6]. This behavior hinders their use to a large extent, in spite of their potential for lightweight structural elements [7].

It has recently been shown that alloying with certain rare-earth (RE) elements might lead to a complete elimination of the RT yield anisotropy and asymmetry in wrought Mg alloys [8–12]. RE additions influence dynamic recrystallization during processing and lead to weak deformation textures [8–10]. However, some studies [11,12] suggest that such weak textures alone cannot explain the isotropic mechanical behavior and that changes in the CRSSs of the different deformation modes with respect to non-RE Mg alloys must also concur. These changes have not been quantified to date and the origin of the influence of the RE elements on the CRSS values for Mg alloys is currently not fully understood.

In this work, the values of CRSSs of the extruded alloys Mg–1% Mn–0.5 wt%Nd (MN10) and Mg–1%Mn–1 wt%Nd (MN11) are obtained by an inverse optimization strategy [14] from the experimental stress–strain curves of uniaxial tests along different orientations with respect to the extrusion axis (ED). The optimization method is based on computational homogenization of the polycrystal behavior by means of crystal plasticity finite element (CPFE) simulations of a representative volume element (RVE) of the microstructure. The result of the optimization is the set of CRSSs that lead to the best agreement between experimental results and the corresponding numerical simulations. Thus, the effect of Nd on the CRSSs can be quantified by comparing the values obtained for MN10 and MN11 Mg alloys with those corresponding to pure Mg.

The MN10 and MN11 alloys were gravity cast to produce billets for extrusion with a diameter of 93 mm. The billets were homogenized at 350 °C during 15 h before processing. Then, indirect extrusion of MN10 and MN11 billets was carried out at 360 °C and 350 °C, respectively, at 2.8 mm/s, to produce round bars of 17 mm in diameter (extrusion ratio equal to 1:30), which were subsequently air-cooled. Uniaxial tension and compression tests were

performed on the as-extruded bars at RT and at an initial strain rate of $10^{-3}\,s^{-1}$ using an Instron universal testing machine. Dog-bone tensile specimens, with gauge dimensions of 4 mm in diameter and 12 mm in length, were machined with their loading axis parallel to the extrusion direction (ED). The compressive specimens were cylinders with 3 mm in diameter and 4.5 mm in length machined with their loading axis parallel to the ED, inclined 45° towards the ED and perpendicular to the ED. The microstructure was studied by optical microscopy (OM) in an Olympus BX-51 microscope. The metallographic preparation consisted of several grinding and polishing steps followed by chemical etching in a solution based on picric and acetic acids in order to reveal grain boundaries. The macrotexture was measured by X-ray diffraction (XRD). The (0001), $(10\bar{1}0)$, $(10\bar{1}1)$, $(10\bar{1}2)$, $(10\bar{1}3)$ and $(10\bar{1}0)$ pole figures were measured using Cu Kα radiation in a XPert PRO ALPHA1 PANalytical diffractometer furnished with a PW3050/60 goniometer. From these experimental data, the ODF and the pole figures were obtained using the MATLAB toolbox MTEX [15]. The inverse pole figures were then derived from the direct pole figures.

The effective behavior of MN10 and MN11 Mg alloys was determined through the CPFE simulation of an RVE of the polycrystalline microstructure. The crystal plasticity model of each grain is presented in detail in [14] and accounts for the dominant deformation modes of Mg alloys: basal $\langle a\rangle$, prismatic $\langle a\rangle$ and pyramidal $\langle c+a\rangle$ slip as well as tensile twinning. Each slip and twinning mode is characterized by a CRSS function that evolves with accumulated shear strain on the different systems. The shape of this function for each deformation mode is defined using three parameters, namely the initial and saturation CRSSs (τ_0, τ_s) and the initial hardening modulus h_0.

The polycrystalline RVEs are cubic volumes discretized with cubic finite elements [16]. RVEs with different levels of complexity were used: from simple RVEs where each cubic element represents a grain (125, 512 and 1000 crystals per RVE were used) to complex RVEs which provide a realistic representation of the grain size and shape within the polycrystal. The RVEs for these latter models were generated using Dream3D [17]. An equiaxed grain shape was chosen and the grain size distribution followed a log-norm function. The realistic models included 300 grains with approximately 200 voxel elements per grain (Fig. 1). The grain orientations in all RVEs were determined from the experimental orientation distribution function (ODF) of the initial texture. The orientation of each grain was obtained by a Monte Carlo lottery and the larger the number of grains, the higher the accuracy in the model texture.

The mechanical behavior of the polycrystalline RVE under a given deformation history was obtained by the finite element method using periodic boundary conditions. The single crystal behavior is dictated by a set of parameters $\boldsymbol{\beta}$, which defines the evolution of the CRSS of the slip and twinning modes considered (τ_0, τ_s and h_0 for each deformation mode). An objective error function $O(\boldsymbol{\beta})$ can be built from the experimental stress–strain curves and the corresponding numerical simulations according to

$$O(\beta) = \sum_{i=1}^{n} |y_i - f(x_i, \beta)|$$

where (x_i, y_i) stands for a set of n points defining the experimental stress–strain curves and $(x_i, f(x_i, \boldsymbol{\beta}))$ are the corresponding points obtained by computational homogenization. An inverse optimization strategy based on the Levenberg–Marquardt method was used to find the set of parameters $\boldsymbol{\beta}$ that minimizes the objective error function $O(\boldsymbol{\beta})$ [14]. The optimization procedure is highly non-linear and began using a simple RVE in which each grain is represented by one voxel. The number of crystals in the RVE increased progressively (125, 512 and 1000) once the optimization algorithm has reached the optimum solution for each RVE. Final optimization was carried out with the complex RVE in Fig. 1. This hierarchical strategy was very efficient and reduced considerably the computational resources necessary to carry out the optimization.

The as-extruded MN10 and MN11 round bars were fully recrystallized and their microstructure was formed by equiaxed grains with average diameters of 21 μm and 17 μm, respectively. The initial texture of both alloys, measured at the center of the bars, is shown in Fig. 2 by means of inverse pole figures. Both textures are weaker than those typical of extruded non-RE containing Mg alloys [6]. The weak texture is especially pronounced in the MN11 bar while a slight tendency for the ED to be aligned in the $\langle 10\bar{1}0\rangle$ direction is still observed in the MN10 bar. The origin of this weak texture is still under debate. It has been proposed that, in RE-containing alloys, there is a larger tendency for recrystallized grains to nucleate at shear bands and that the orientations of such nuclei become more widely spread as the Nd content increases [13]. It has also been suggested that the presence of RE solutes and intermetallic particles hinder the grain boundary mobility, thereby delaying the preferred growth of certain

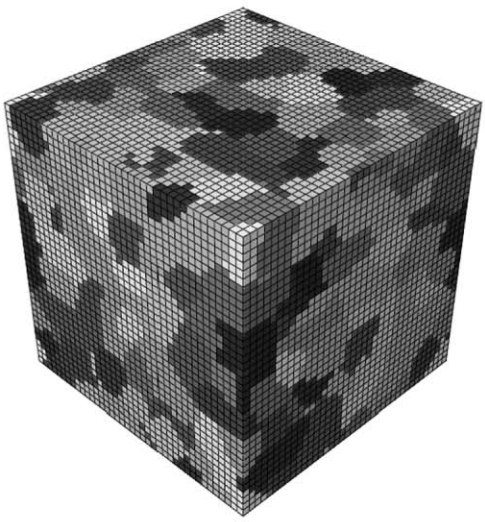

Fig. 1. Cubic RVE of the microstructure including 300 crystals discretized with 200 cubic finite elements per grain.

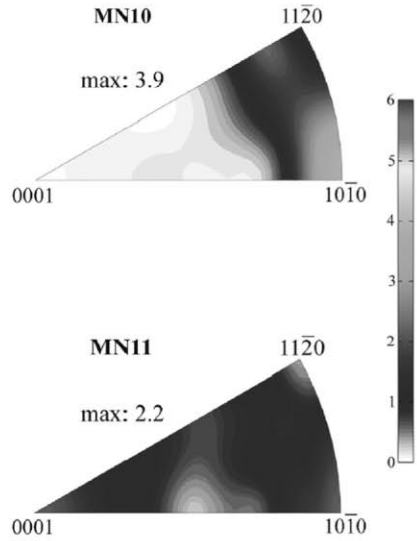

Fig. 2. Inverse pole figures showing the orientation of the extrusion direction of the (a) MN10 and (b) MN11 alloys in the as-extruded condition.

orientations [13] and leading to finer grains with respect to non-RE containing Mg alloys.

The experimental stress–strain curves, corresponding to compression tests parallel and perpendicular to the ED and to tension tests parallel to the ED, are plotted in Fig. 3. They were used as input data in the optimization procedure described above. The MN10 alloy (Fig. 3(a)) exhibits a yield stress asymmetry, albeit less pronounced that that reported for non-RE Mg alloys [18]. In particular, the yield stress in tension along the ED is 1.4 times the compressive yield stress, reflecting the combined effect of twinning polarity and texture, which results in a higher activity of prismatic slip in tension and of tensile twinning in compression. The mechanical anisotropy of the MN10 alloy is also evident by the different shapes of the tension and compression stress–strain curves, the former being concave-up and the latter concave-down. On the contrary, the MN11 alloy exhibits a very isotropic mechanical behavior (Fig. 3(b)). The yield stress is very similar for all the tests and the shape of the curves is always concave-up.

Fig. 3 also includes the stress–strain curves obtained by computational homogenization of the RVE in Fig. 1 with the optimum set of parameters obtained by the optimization procedure. The agreement between experimental and numerical results is remarkable, being the average error (value of objective function divided by the number points) always smaller than 7 MPa per point. This relatively small difference demonstrates the ability of computational homogenization in combination with the inverse optimization strategy to capture the anisotropic mechanical response of Mg alloys. To provide further support for this statement, the fitted model was used to predict an independent compression test performed at 45° with respect to the ED direction in both alloys (Fig. 3(c)). Again, the agreement between experimental and numerical results is good (less than 10 MPa per point), validating the optimization procedure and the set of parameters obtained.

The optimized values of the initial CRSSs, τ_0, for both alloys are shown in Table 1 and compared with those reported recently for pure Mg from single crystal experiments [19]. It can be observed that Nd additions lead to an increase of the initial CRSS of all deformation modes with respect to those of pure Mg. However, the increase in the CRSS was more pronounced for extension

Table 1
Comparison of the initial CRSSs (τ_0) obtained by inverse optimization for the MN10 and MN11 alloys with those measured in pure Mg single crystals [18].

CRSS (τ_0) (MPa)	Pure Mg	MN10	MN11
Basal $\langle a \rangle$	1.75	12	40
Tensile twinning	3.5	24	42
Prismatic $\langle a \rangle$	25	65	46
Pyramidal $\langle c+a \rangle$	40	75	50
$CRSS_{basal}/CRSS_{twinning}$	0.5	0.5	0.95
$CRSS_{prism}/CRSS_{twinning}$	7.1	2.7	1.1
$CRSS_{pyr}/CRSS_{twinning}$	11.4	3.1	1.2

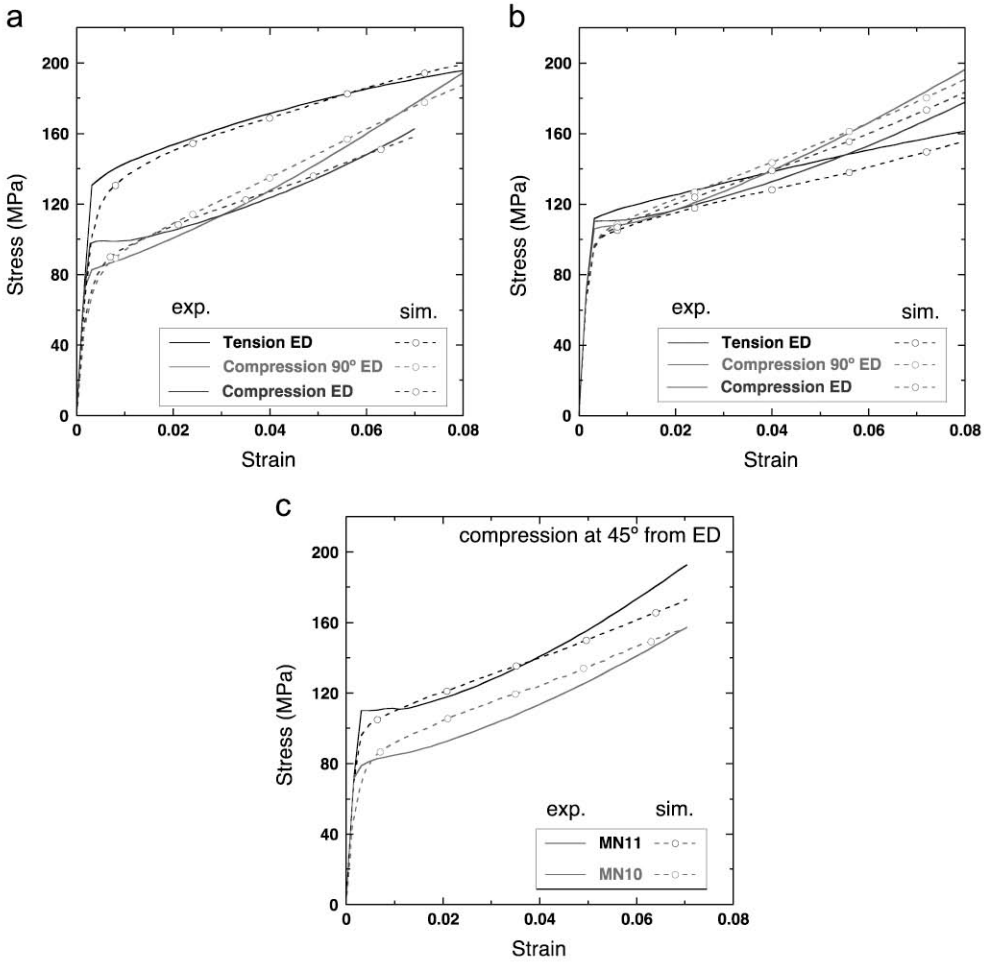

Fig. 3. (a,b) Experimental (solid lines) and simulated (broken lines) stress–strain curves resulting from the optimization procedure for the (a) MN10 and (b) MN11 alloys tested in tension along the ED, in compression along the ED and in compression in a direction perpendicular to the ED. (c) Experimental (solid lines) and simulated (broken lines) stress–strain curves corresponding to both alloys tested in compression at 45° with respect to the ED.

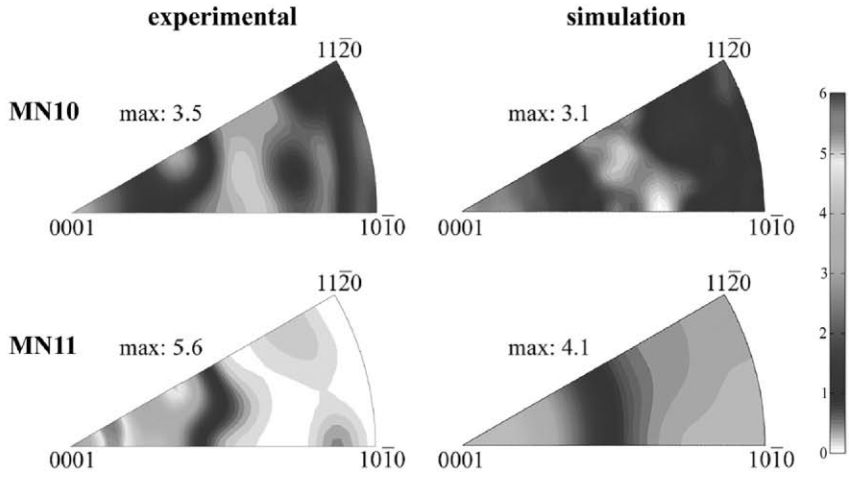

Fig. 4. Experimental and simulated inverse pole figures showing the orientation of the compression direction (CD) of the MN10 and MN11 alloys after uniaxial compression along the ED. The numbers in the legend stand for multiples of random distribution.

twinning and basal slip. Furthermore, the $CRSS_{basal}/CRSS_{twinning}$ ratio increases notably in the RE-containing alloys while the $CRSS_{prism}/CRSS_{twinning}$ and the $CRSS_{pyr}/CRSS_{twinning}$ ratios decrease steeply. These changes are more pronounced in the MN11 alloy, in which similar values of the initial CRSS were obtained for all active slip and twinning systems. This is consistent with the remarkable isotropy in the mechanical behavior of this alloy. The observed variations in the initial CRSS lead to different activities of the slip and twinning systems, as compared with pure Mg. Firstly, the increase of the $CRSS_{basal}/CRSS_{twinning}$ ratio is consistent with an enhancement of twinning at the expense of basal slip, which would give rise to the concave-up shape of all the MN11 stress–strain curves, including that corresponding to the tensile test (Fig. 3(b)). Promotion of twinning in the RE-containing Mg alloys at the expense of basal slip was postulated by Hidalgo-Manrique et al. [13] based on observations of the concave-up shape of the RT tensile stress–strain curves of a similar MN11 alloy and it was attributed to an increase in the $CRSS_{basal}/CRSS_{twinning}$ ratio due to the presence of intermetallic prismatic plates, very effective for hindering basal slip [20]. The present numerical results confirm the hypothesis that the $CRSS_{basal}/CRSS_{twinnig}$ increases [13] and, furthermore, suggest that an addition of 1 wt% of Nd brings the mentioned ratio to a value close to 1. However, since the present alloys have not been age hardened, it is unlikely that the contribution of the precipitates in inhibiting basal slip is very high and the contribution of solute atoms, which are also very effective for hardening basal slip [21], should be much higher.

Secondly, the reduction in the differences of the CRSS between non-basal systems and basal slip and twinning leads to a higher activity of the former. The promotion of non-basal slip has been largely reported for RE-containing alloys [22–25]. However, the actual origin of this behavior is still unclear. In hexagonal close-packed metals, the c/a ratio affects the difference in the CRSS between basal and non-basal slip systems. According to some works [22], RE additions decrease the c/a ratio of Mg and stimulate the activation of non-basal slip systems. It has been also put forward that RE elements influence the Peierls potentials and the stacking fault energy on basal and non-basal planes and therefore lead to a change in the relative CRSSs, resulting in the easier activation of non-basal slip [23,24]. The grain refinement attained in RE-containing alloys may also lead to a higher activity of non-basal slip and not only because the differences in CRSS between basal and non-basal slip decreases with decreasing grain size [25], but also because the non-basal slip systems are active near the grain boundaries, which are regions of stress concentration [26].

The experimental and simulated inverse pole figures of the compression direction (CD) after compression along the ED in the MN10 and MN11 bars are shown in Fig. 4. Both experimental and predicted textures are very similar, evidencing further the validity of the optimization strategy and the calculated values of CRSSs. The CD tends to align mostly with the c-axis in both alloys after deformation, and, less notably, with a pyramidal direction along the $\langle 0001\rangle$–$\langle 11\bar{2}\bar{0}\rangle$ symmetry boundary of the stereographic triangle. This is consistent with a large activity of twinning in both bars, especially in the weakly textured MN11 alloy, which leads to an 86° reorientation of those grains with the c-axis inclined less than 45° towards the CD. Afterwards, grains with basal orientations undergo a rotation towards the $\langle 11\bar{2}\bar{0}\rangle$ pole owing to pyramidal slip.

In summary, the inverse optimization strategy developed in [14] allowed to obtain the CRSS values for the alloys MN10 and MN11 (with 0.5 wt% and 1 wt% Nd, respectively) from macroscopic testing results. The initial CRSSs were observed to change drastically with increasing RE content. In particular, the CRSSs of basal and twinning modes as well as the $CRSS_{basal}/CRSS_{twinning}$ ratio increases, while the $CRSS_{prism}/CRSS_{twinning}$ and $CRSS_{pyr}/CRSS_{twinning}$ ratios decrease to an extent that all values become similar for alloying additions of 1 wt%. This is consistent with the isotropic yielding behavior observed in the MN11 alloy. These changes in CRSSs with RE addition lead to the promotion of twinning at the expense of basal slip and to an enhanced activity of non-basal systems.

Acknowledgments

Financial support from the PRI-PIBUS-2011-0917 and PRI-PIBUS-2011-0990 Projects (MAGMAN), funded by the Spanish Ministry of Economy and Competitiveness (MINECO), is gratefully acknowledged. The authors also thank Vanesa Martínez for assistance with the mechanical tests and Ignacio Carabias (UCM CAI Difracción de Rayos X) for his kind support with macrotexture measurements.

References

[1] Partridge PG. Metall Rev 1967;12:169–94.
[2] Barnett MR. Metall Mater Trans A 2003;34:1799–806.
[3] Munroe NM, Tan X, Gu H. Scr Mater 1997;36:1383–6.
[4] Christian JW, Mahajan S. Prog Mater Sci 1995;39:1–157.
[5] Ulacia I, Dudamell NV, Gálvez F, Yi S, Pérez-Prado MT, Hurtado I. Acta Mater 2010;58:2988–98.

[6] Dillamore IL, Roberts WT. Metall Rev 1965;10:271–380.
[7] Polmear IJ. Mater Sci Technol 1994;10:1–16.
[8] Ball EA, Prangnell PB. Scr Metall Mater 1994;31:111–6.
[9] Mackenzie LWF, Davis B, Humphreys FJ, Lorimer GW. Mater Sci Technol 2007;23:1173–80.
[10] Stanford N, Barnett MR. Mater Sci Eng A 2008;496:399–408.
[11] Robson JD, Twier AM, Lorimer GW, Rogers P. Mater Sci Eng A 2011;528:7247–56.
[12] Hidalgo-Manrique P, Yi SB, Bohlen J, Letzig D, Pérez-Prado MT. Metall Mater Trans A 2014, http://dx.doi.org/10.1007/s11661-013-2169-x, in press.
[13] Hidalgo-Manrique P, Yi SB, Bohlen J, Letzig D, Pérez-Prado MT. Metall Mater Trans A 2013;44:4819–29.
[14] Herrera-Solaz V, LLorca J, Dogan E, Karaman I, Segurado J. Int J Plast 2014;57:1–15.
[15] Bachmann F, Hielscher R, Schaeben H. Solid State Phenom 2010;160:63–8.
[16] Segurado J, LLorca J. Comp Mater Sci 2013;76:3–11.
[17] Dream.3d, ⟨http://dream3d.bluequartz.net⟩; 2012.
[18] Yi S, Davies CHJ, Brokmeier HG, Bolmaro RE, Kainer KU, Homeyer J. Acta Mater 2006;54:549–62.
[19] Zhang J, Joshi SP. J Mech Phys Solids 2012;60:945–72.
[20] Nie JF. Scr Mater 2003;48:1009–15.
[21] Akhtar A, Teghtsoonia E. Acta Metall 1969;17:1339–49.
[22] Agnew SR, Yoo MH, Tomé CN. Acta Mater 2001;49:4277–89.
[23] Chino Y, Kado M, Mabuchi M. Mater Sci Eng A 2008;494:343–9.
[24] Sandlobes S, Zaefferer S, Schestakow I, Yi S, Gonzalez-Martinez R. Acta Mater 2011;59:429–39.
[25] Stanford N, Barnett MR. Int J Plast 2013;47:165–81.
[26] Koike J, Kobayashi T, Mukai T, Watanabe H, Suzuki M, Maruyama K, et al. Acta Mater 2003;51:2055–65.